doi:10.26443/seismica.v5i1.1794

Moment tensor solutions and stress regime along the Northern Caribbean plate boundary off southeastern Cuba

O. González *[1,2,3], **E. Arango** [1,2], **E. Calais** [4,5], **V. Clouard** [2], **B. Moreno** [1,2], **R. Palau** [1], **J. Corbeau** [3]

[1]Centro Nacional de Investigaciones Sismológicas (CENAIS). Ministerio de Ciencia, Tecnología y Medio Ambiente, Cuba., [2]Géosciences Environnement Toulouse (GET), Observatoire Midi-Pyrénées (OMP), Université de Toulouse III Paul Sabatier, France., [3]Observatoire Volcanologique et Sismologique de Martinique. Institut de Physique du Globe de Paris, France., [4]Département de Géosciences, École normale supérieure, Université PSL, Paris, France., [5]Université Côte d'Azur, Observatoire de la Côte d'Azur, Géoazur, France

Author contributions: *Conceptualization*: González, Clouard, Calais, Palau. *Data Curation*: González, Palau, Moreno, Corbeau. *Formal*: Analysis. *Funding Acquisition*: Calais, Clouard, González. *Investigation*: All coauthors. *Methodology*: González, Calais, Palau, Clouard. *Writing – original draft*: Gonzalez, Calais, Clouard, Corbeau, Arango. *Writing – review & editing*: All coauthors.

Abstract For a better understanding of the kinematics and mechanics of the Oriente transform fault, a left-lateral boundary along Cuba's southern margin in the Caribbean, we use the seismic records to determine new deviatoric moment tensor solutions by full waveform inversion for 49 earthquakes, magnitude range 6.8 > M > 3.5, along the southeastern coast of Cuba, from 2015 to the end of 2024. We validate our results using 14 events with moment tensors independently determined by other agencies. The moment tensor solutions calculated here, together with 16 historical ones from the gCMT database, highlight the along-strike segmentation of the Oriente fault system, with oblique normal faulting in the Cabo Cruz transtensional stepover, and oblique reverse faulting further east in the Oriente Deep Zone and the transpressional Santiago Deformed Belt. The Oriente fault, though largely strike-slip, may have a small reverse component itself, as exemplified by the November 10, 2024, Mw 6.8 earthquake. The bulk of reverse/oblique faulting earthquakes, however, coincide with the Santiago Deformed Belt, a narrow crustal sliver overthrusting to the south the extended island arc crust of the eastern Cayman Trough and likely bounded to the north by the Oriente fault. The moment magnitudes computed agree well with the local magnitudes for Mw > 4, as expected. For Mw < 4, we find Mw ≈ 0.67 ML, similar to other regions, for instance the Lesser Antilles.

Production Editor: Gareth Funning
Handling Editor: Robert Skoumal
Copy & Layout Editor: Hannah F. Mark

Signed reviewer(s): Jiri Zahradnik

Received: June 25, 2025
Accepted: March 25, 2026
Published: April 30, 2026

1 Introduction

The island of Cuba results from the collision of the Great Arc of the Antilles (Burke, 1988), a volcanic arc that developed as a result of the subduction of the proto-Caribbean oceanic domain under eastern edge of the Caribbean plate, with a passive segment of the North American plate margin in the Campanian (Iturralde-Vinent, 1996; Iturralde-Vinent et al., 2016). This collision accreted the volcanic arc and its basement, together with ophiolitic fragments of the proto-Caribbean domain, onto the passive margin, forming a fold belt whose remnants are also found in Hispaniola and Puerto Rico (e.g. García-Casco et al., 2008). The late Paleocene-Eocene was marked by a drastic change in the kinematics of the Caribbean plate, with the opening of the Yucatan basin, then the successive activation of left-lateral strike-slip faults – Trocha, Cauto, then Oriente – which permitted the eastward motion of the Caribbean plate with respect to North America and the opening of the Cayman Trough oceanic pull-apart basin from 40 My onward (e.g., Mann and Burke, 1984; Mann et al., 1995; Leroy et al., 2000).

In the present day, the island of Cuba, long incorporated into the North American plate, concentrates most of its seismicity along the Oriente plate boundary fault, including 85% of the largest events (M ≥ 7.0; e.g., 1766, 1852, 1992, 2020) (Álvarez et al., 1999). The Oriente fault system is a left-lateral transform fault which marks the boundary between the North American plate to the north and the Gonâve microplate (Mann et al., 1995) (Figure 1). It initiates at the northern tip of the mid-Cayman spreading center, bounds the Cayman ridge and the margin of eastern Cuba to the south, then continues eastward through the Windward Passage, along the northern coast of Haiti and into the Cibao Valley in the northern part of the Dominican Republic where it is termed "Septentrional fault" (Calais and de Lepinay, 1991). The Oriente fault geometry and structure, display a discontinuous trace composed of several fault segments, pull-apart basins, and zones of active compression (Calais and de Lepinay, 1991); therefore, it can be regarded operationally as a composite fault system that accommodates regional deformation. Other potentially active faults have been identified in Cuba, such as Cauto-Nipe, La Trocha, and Pinar (e.g. Álvarez et al., 1985; Cotilla Rodriguez et al., 2007; García et al., 2003; Vega-Garriga et al., 2022) (Figure 1). Based on historical earthquakes the Oriente Fault System is the most

*Corresponding author: oleary@cenais.cu

seismically active, with 23 of the 29 earthquakes in the Cuban region with intensities exceeding VII (EMS) (Álvarez et al., 1999; Van Dusen and Doser, 2000).

Along the southeastern coast of Cuba, the Oriente Fault System bounds the Paleogene volcanic arc of the Sierra Maestra and other older accreted terranes to the north, with the extended volcanic arc crust of the Cayman basin to the south. This fault system accommodates about half of the eastward motion of the Caribbean plate with respect to North America (DeMets et al., 2000), the other half being accommodated by the Walton-Enriquillo fault system along the southern edge of the Cayman Trough (Symithe et al., 2015). The two faults isolate the Gonâve microplate (Mann et al., 1995), whose present-day motion is parallel to the strike of the Oriente fault (Benford et al., 2012). Recent GNSS measurements in Cuba confirm this strike-slip kinematics along the offshore margin of southeastern Cuba (Calais et al., 2023). Off the western tip of the eastern Cuban margin, the Oriente fault forms a tensional step-over, which coincides with the Cabo Cruz pull apart basin. To the east, the Oriente fault bounds a narrow and deep basin (Oriente Deep Zone, up to 7700 m depth), which pinches out eastward, as the compressional Santiago Deformed Belt develops (Calais and de Lepinay, 1991). The Santiago Deformed belts affects recent sediments of the eastern half of the Oriente Deep, then involves margin basement further east. The frontal, south-verging thrust of the Santiago Deformed Belt is disconnected, at the surface, from the Oriente Fault per se, which runs parallels to it but to the north, through the margin slope. They may merge at depth in the form of a half flower structure (e.g., Sylvester, 1988), though this structure has not yet been imaged directly at depth, except through seismic reflection profiles that penetrate no more than 2-3 km into the crust.

The distribution of seismicity and type of focal mechanisms reflect the segmentation of the Oriente plate boundary fault system with (1) pure strike-slip events west longitude of -78 (Cabo Cruz basin), (2) a lack of significant events along the Cayman ridge segment of the Oriente fault, i.e., west of -78, until that gap was filled by the rupture of the 28/01/2020, Mw 7.7 earthquake (Calais et al., 2025), (3) normal faulting or strike-slip/normal faulting events coincidental with the Cabo Cruz transtensional basin, and (4) a variety of source mechanisms east of Cabo Cruz basin, mostly mixed with a compressional component (Calais et al., 1998; Moreno et al., 2002). However, understanding the kinematics of this latter segment of the Oriente Fault System, together with the significance of the compressional Santiago Deformed Belt in an apparently purely strike-slip context, requires additional analysis. Here we contribute to the seismotectonic description of the Oriente Fault System by determining new moment tensor solutions using full waveform inversion. This technique has become routine practice at many observatories, facilitated by the availability of high-quality seismic data and advanced computing techniques (e.g., Havskov and Ottemöller, 2010). However, apart from the Harvard CMT catalog, only a few isolated moment tensor solutions for Cuban earthquakes have been published (e.g., González et al., 2015, 2021). In this study, we used data from the recently upgraded seismic network of the Cuban National Seismological Service (SSNC), complemented by five temporary broadband stations from Epos-France's Sismob mobile seismological park (sismob.epos-france.fr), deployed from 2018 to 2019 (Clouard, 2018), as part of the Interreg PREST project (Regional Telluric Surveillance Platform, https://www.interreg-caraibes.com/prest), along with regional stations (see Supplementary Information #1 for details), to compile a comprehensive moment tensor catalog for moderate-magnitude earthquakes between 2015 and the end of 2024, providing new insights into the seismotectonics of the Northern Caribbean plate boundary in southeastern Cuba.

2 New moment tensor database

2.1 Data and method

We used data from the Cuban seismic catalog to identify earthquakes with M > 3.5 and whose signal was recorded by regional broadband, 3-component seismic stations (Figure 1). From this dataset, we define two subsets of earthquakes for further analysis: (1) a calibration set of 14 earthquakes, with moment tensor solutions from the gCMT catalog (Dziewonski et al., 1981; Ekström et al., 2012), a long-running, global effort commonly used in the scientific literature, serves for calibration purposes; (2) a database of 35 earthquakes located within our study area, with a good signal to noise ratio in the frequency band for the regional waveform inversion, typically from 0.02 to 0.1 Hz (Dreger, 2003), for which the moment tensor was unknown. The seismotectonic interpretation of the results then includes both datasets.

For earthquake-station paths crossing predominantly the Gonâve microplate and eastern Cuba, we perform the waveform inversion using the 1D structural model of Moreno et al. (2002) (see values in Supplementary Information #2). This model is routinely employed by the SSNC for earthquake location in the Cuban region and has demonstrated consistency with the physical properties of the crust and upper mantle structure derived from regional S- and surface-wave tomography (González et al., 2011, 2012). For longer earthquake-station paths, crossing other types of crustal structures, such as the interior of Cuba or Hispaniola island, we used the alternative 1D velocity model of Dorel (1978), as employed by Corbeau et al. (2019) for the Gulf of Gonâve. This model, derived from seismic refraction profiles averaged for land and oceanic regions, comprises three crustal layers that are 3, 12, and 15 km-thick, with Vp of 3.5, 6.0, and 7.0 km/s respectively, with an underlying mantle model represented by a half space with Vp=8.0 km/s.

Density values for both models come from the relationship of Nafe and Drake (1960), while the attenuation quality factors Qp and Qs are determined by the regression of Graves and Pitarka (2004). The earthquake parameters are those from the SSNC catalog (https://www.cenais.gob.cu/navegador/), and the instrument

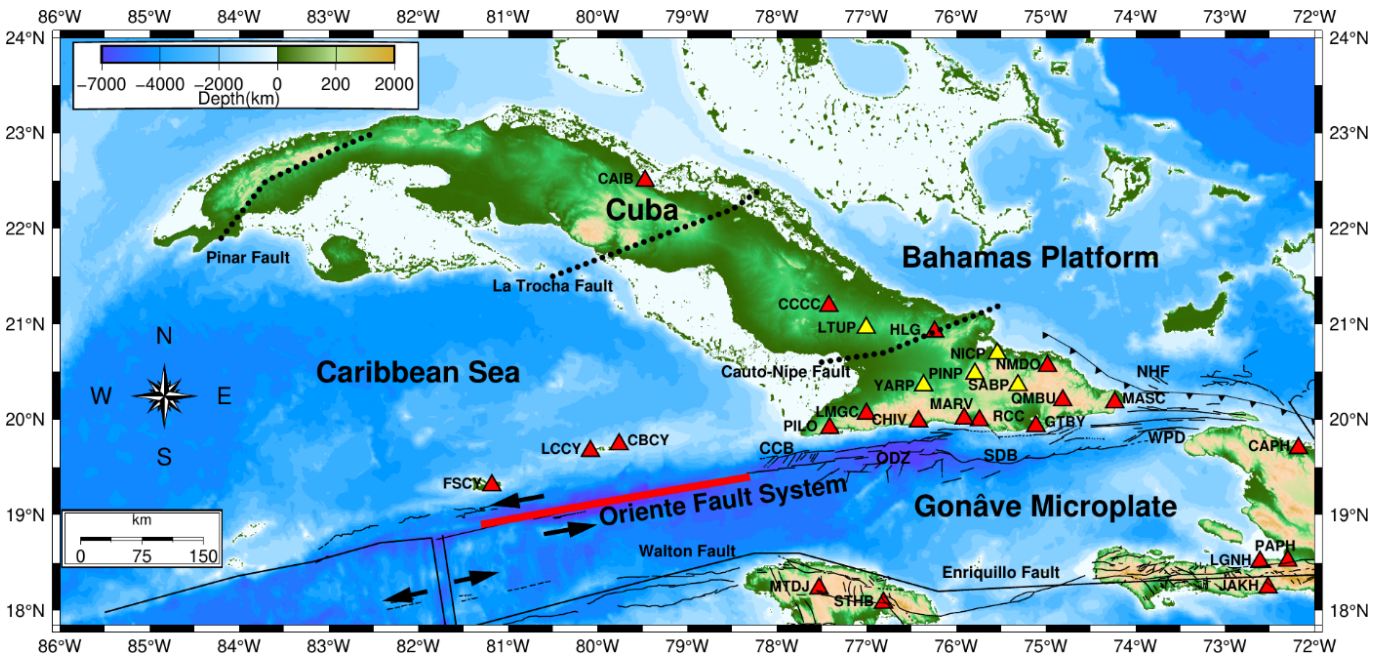

Figure 1 Location map of the 29 seismic stations used in this study and some principal faults in Cuba (modified from García et al., 2003). CCB, Cabo Cruz Basin; ODZ, Oriente Deep Zone; SDB, Santiago Deformed Belt; WPD, Windward Passage Deep and NHF, Northern Hispaniola Fault. Red triangles, permanent seismic stations; yellow triangles, temporary seismic stations from Interreg PREST project (see Table in Supplementary Information #1 for the associated network codes and type of instruments). Red line represents the rupture area of the 28/01/2020, Mw 7.7 earthquake (Calais et al., 2025).

response parameters come from the IRIS Data Center (https://ds.iris.edu/SeismiQuery/responses.htm) and from Epos-France's Sismob mobile seismological park (https://seismology.resif.fr/). We verified that sensor orientation was correct using the 3-component P-polarities and azimuths following Havskov and Ottemöller (2010).

In order to select the optimum frequency band for the inversion, we initially evaluate each component in several frequency bands using the SAC software (Goldstein, 1999). We use the ISOLA codes (Sokos and Zahradnik, 2008, 2013) to calculate the signal to noise ratio (SNR) of the events and to identify and remove the records spoiled by instrumental disturbances (Zahradník and Plešinger, 2005; Zahradnik and Plesinger, 2010; Vacka et al., 2015). We require at least 10 usable components and a SNR ≥ 2 in the inverted frequency band in order to validate events.

We compute the deviatoric moment tensors using ISOLA, which uses a full waveform inversion with the least-squares method, while the centroid position and time are grid-searched. The spatial grid search is performed first vertically below the epicenter in an interval around the hypocenter depth with steps of 1 km, and in an interval of 3 s around the origin time with steps of 0.09 s. The second grid search is usually performed in a horizontal plane with typical steps ranging from 2 to 4 km, fixing the reference depth from the first search. The best-fitting solution is characterized by its variance reduction percentage (VR), or correlation (where correlation squared equals VR), its double-couple percentage (DC), and its condition number (CN). CN serves for relative evaluation of the moment-tensor resolvability: the lower CN, the better resolvability (for complete definitions, see Krizova et al., 2013).

We then check all final moment tensor solutions using the P-polarities of the vertical components. Inversion results are considered valid only when over 70% of the P polarities agree with the solution, under the previously mentioned parameters and conditions. The rejected solutions are recalculated after a full revision of the earthquake basic parameters, of the filtering, and of the analysis of the coherence of the structural model used with the earthquake location. We finally classify the focal mechanisms according to the standard typology of Kaverina et al. (1996), as implemented in the FMC codes of Álvarez Gómez (2019).

2.2 Calibrations set

To evaluate the validity of the input parameters used (filtering, instrumental calibration, and velocity model), we calculated moment tensor solutions for 14 earthquakes previously determined by gCMT (Dziewonski et al., 1981; Ekström et al., 2012) using the same parameters, procedures, and local and regional stations as in this study (Table 1 and See Supplementary Information #3 for detailed results for each earthquake). Due to the magnitude range of these events, with Mw > 4.6, the frequency band was set between 0.02 and 0.07 Hz, consistent with the methodology used in similar studies (e.g., González et al., 2017; Dreger, 2003).

For nine earthquakes, the recalculated magnitudes differed slightly from the gCMT catalog, by less than 0.2, with seven showing lower Mw. Such small differences, particularly higher values in gCMT for Mw < 5.5, have also been observed when comparing gCMT magnitudes to those from several seismological services in Northern and Central America (Di Giacomo et al., 2021). Factors contributing to these discrepancies may include

difference in crustal models, station distribution and distance relative to the hypocenter, and signal-to-noise ratio (Konstantinou and Rontogianni, 2011; Patton and Randall, 2002). These issues are especially relevant in the study area, where station distributions (Figure 1) and the Earth's interior structure for the earthquake-station paths can vary significantly (González et al., 2012). We compared the recalculated focal mechanisms with their corresponding gCMT solution using the method of Kagan (1991) and find for all earthquakes relatively low Kagan angles (K ≤ 32°; Table 1), indicating a good agreement between our solution and that of gCMT.

2.3 New regional moment tensors

We now turn to the 35 earthquakes of the study area for which we calculated a new moment tensor solutions using the full-waveform inversion described above (Figure 2, Table 2, and detailed results for each earthquake in the Supplementary Information #4). The solutions selected met criteria of variance reduction VR > 50%, double-couple percentage DC > 50%, and condition number CN < 5, and consistency with the P-polarity analysis. In the following, each event is identified by a number that appears on Tables 1, 2, and Supplementary Information #5.

Two earthquakes have VR less than 50% and DC values less than 50%, numbered 6 and 17 in Table 2. However, their CN values less than 4.5, high signal to noise ratio (SNR), and adequate number of components (NC) do not indicate the presence of an ill-posed inversion problem. Additionally, both waveform inversions show a good agreement with a P-polarities analysis (Supplementary Information #6). We hence decided to included them in the database.

In the new database, 13 moment tensor solutions have significant non-DC component (> 40%). This feature is also present is some of the gCMT solutions. Large non-DC components may be associated with artifacts of the inversion process (Rösler et al., 2024), limited azimuthal coverage of seismic stations (Kumar et al., 2015), or natural causes such as fault complexity (Yue and Lay, 2020) and volumetric changes in the source area linked to fluid-triggered seismicity (Vavryčuk, 2002). However, current evidence does not allow a definitive distinction between these possibilities, and resolving such causation is beyond the scope of this study. Nevertheless, the presence of large non-DC components does not affect the seismotectonic interpretations presented herein regarding the focal mechanism classification.

Mw values from this study closely match the local magnitudes (ML) routinely computed by the SSNC for 4 ≤ ML ≤ 6 (Figure 3), consistent with Kanamori (1983). For smaller events (ML < 4), Mw follows Mw ≈ (2/3)ML + 1.54, in agreement with Munafò et al. (2016) and with coefficients similar to those calculated for the Lesser Antilles, (e.g. González et al., 2017).

3 Seismotectonic implications

In general, the moment tensor solutions determined here match previous observations from less populated databases (Calais et al., 1998; Van Dusen and Doser, 2000; Moreno et al., 2002). Figure 4, which uses the standard typology of Kaverina et al. (1996), shows that reverse, oblique and strike slip focal mechanisms are predominant in the study area. Most of the events are distributed within the Cabo Cruz basin, along the Oriente Deep Zone, and in the Santiago Deformed Belt (Figure 2). We describe each area below and use the focal mechanisms to solve for regional stress tensors using the STRESSINVERSE code of Vavryčuk (2014). This iterative inversion method has the advantage of identifying the nodal plane more susceptible to failure through the implementation of a fault instability constraint. Hence, it does not require prescribing *a priori* which of the two nodal planes is the actual fault, and provides quantitative information on the consistency of the focal solutions with a single stress tensor estimate. The uncertainties associated with the azimuth and plunge of the principal stress axes (σ_1, σ_2, σ_3) are estimated. The relatively low values indicate that the uncertainties do not significantly affect the classification of the stress regime based on the plunge ranges. A summary of the main inversion results for each area is provided in Supplementary Information #7.

3.1 Cabo Cruz Basin

Newly-determined moment tensor solutions 7c, 10c, and 17 correspond to events that occur within the Cabo Cruz Basin (Figure 2a), a region that also includes previously-determined moment tensor solutions 5*, 7*, 8*, 9*, and 14* (Perrot et al., 1997; Álvarez et al., 1999) (for the tectonics analysis the 16 historical moment tensor from the gCMT database were included, Supplementary Information #5). The four newly-determined moment tensor solutions 7c and 10c, as well as earlier ones such as 7* and 8* from gCMT, have strike angle of ~240° and dipping angle of ~40°. All of them, including event 17 and 5*, 9* and 14* from gCMT, are indicative of strike-slip faulting, or normal faulting with a significant strike-slip component. These features are consistent with focal mechanisms determined from P-wave first motion polarities by Moreno et al. (2002) and match the normal faults that delimit the series of horsts and grabens oblique to the general trend of the Oriente fault mapped in the seafloor at this tensional step-over in the Oriente fault trace (Calais and de Lepinay, 1991). The stress inversion of all focal mechanisms of this area shows a transtensional regime (Figure 5a) consistent with the focal mechanism of the largest events, such as 7* and 9*.

3.2 Oriente Deep Zone

In the 77.4°W to 76.3°W longitude range, the Oriente Deep Zone (Figure 2b) includes events 6c, 9c, 12c, 12*, 13c, 14c, 14, 15, 16, 19, and 27-35. Prior to earthquake 12c of Mw 5.8 on November 11, 2024, reverse faulting was predominant with fault planes oriented E-W to NW-SE. This event (12c), likely a foreshock of event 13c with

Event #	Origin time yyyymmdd hh:mm:ss.ss	Lat Lon Depth (centroid this study)	Δ (km)	ML	Mw gCMT	Mw this study	Moment Tensor (deviatoric) gCMT	Moment Tensor (deviatoric) this study	DC % this study	VR % this study	CN this study	K °
1c	20160117 06:37:27.20	19.77 -76.07 9	51	4.7	4.9	5.0			55	58	3.6	16
2c	20160117 08:17:34.90	19.78 -76.10 8	42	4.6	4.9	4.9			74	54	5.2	11
3c	20160117 08:30:23.00	19.78 -76.09 7	42	5.0	5.1	5.1			80	67	3.5	13
4c	20160125 18:05:54.40	19.77 -76.07 11	48	4.5	4.8	4.7			64	74	2.4	30
5c	20160930 23:06:48.20	19.79 -74.36 44	31	4.8	4.9	5.0			66	56	2.5	10
6c	20170117 09:08:00.50	19.77 -76.76 9	88	5.5	5.8	5.7			95	46	4.7	12
7c	20171109 03:19:14.50	19.58 -78.10 7	71	4.3	4.8	4.6			71	74	3.0	8
8c	20200429 10:22:49.80	20.17 -74.17 12	70	4.8	4.7	4.6			86	58	2.2	10
9c	20200517 20:47:14.50	19.69 -76.51 12	29	4.2	4.7	4.6			56	79	3.1	29
10c	20200724 19:11:49.70	19.37 -78.19 3	143	4.7	5.1	5.1			94	53	5.5	32
11c	20230216 06:50:44.00	19.57 -73.69 38	135	5.4	5.5	5.5			74	61	2.4	20
12c	20241110 15:50:02.0	19.80 -76.98 15	105	6.0	5.9	5.8			75	83	2.4	15
13c	20241110 16:49:50.0	19.80 -77.08 26	117	6.6	6.8	6.6			77	57	2.7	22
14c	20241223 06:00:56.0	19.80 -76.64 30	99	6.1	5.8	5.8			82	61	2.7	3

Table 1 Comparison of the inversion results of this study (Set 1) and from gCMT (Dziewonski et al., 1981; Ekström et al., 2012). Δ is hypocentral distance of the nearest station used for the inversion; DC is the percent of the double couple and VR the variance reduction and K is the Kagan-angle deviation of our result from gCMT.

Mw 6.8, which occurred an hour later about 5 km to the west, as well aftershocks 28-30 and 33, all show mechanisms that are mostly strike-slip. Other aftershocks however show thrust faulting (32, 34 and 35) or combined fault with considerable strike-slip component (27 and 31). Event 14c of Mw 5.8 could also be considered a large aftershock although it is located relatively farther away, possibly resulting from stress redistribution following the mainshock (van der Elst and Shaw, 2015). Its rake differs from that of other aftershocks in the sequence, suggesting a distinct fault plane or fault slip behavior.

This area, first considered as a pull-apart basin (Mann and Burke, 1984), then as a transition between the

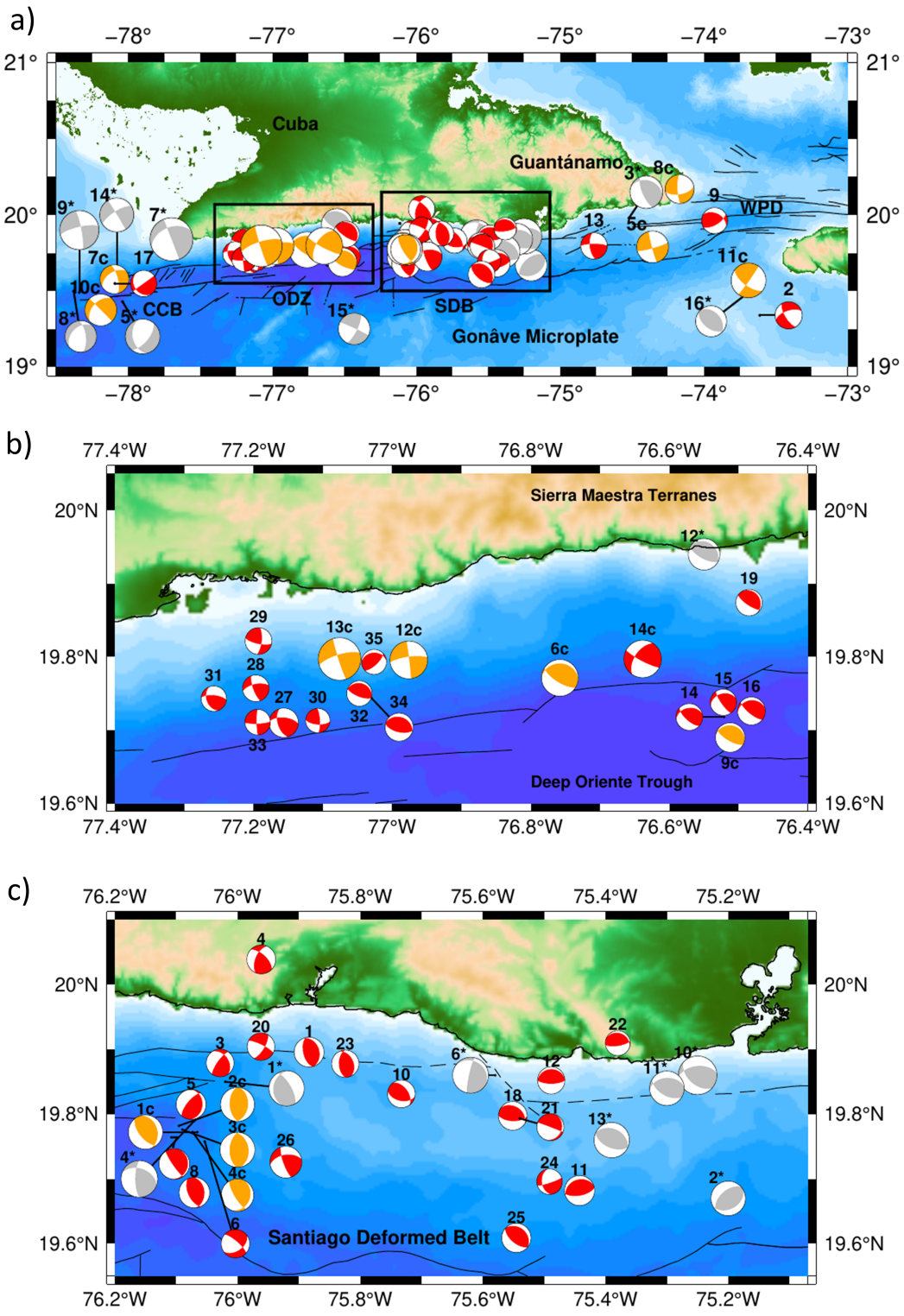

Figure 2 Focal mechanisms of earthquakes in the eastern region of Cuba used in this study. Orange beachballs represent the calibration dataset (our solutions), red beachballs indicate newly determined focal mechanisms, and grey beachballs correspond to older earthquakes from the gCMT database (solution denotated by number with asterisk, see Supplementary Information #5). (a) The complete database; (b) focal mechanisms within the Oriente Deep Zone (ODZ); and (c) focal mechanisms in the Santiago Deformed Belt (SDB). CCB, Cabo Cruz Basin; ODZ, Oriente Deep Zone; SDB, Santiago Deformed Belt; WPD, Windward Passage Deep.

transtensional Cabo Cruz basin and the compressional Santiago Deformed Belt (Moreno et al., 2002), is classically expected to show strike-slip faulting. The moment tensor solutions obtained here are consistent with strike-slip faulting but also indicate a component of reverse faulting, as exemplified by event 13c with Mw 6.8. The inversion of focal mechanisms for a stress tensor is consistent with combined strike-slip and thrust faulting regime for this area (Figure 5b). This compression is expressed locally in the seafloor geology by the active fold-

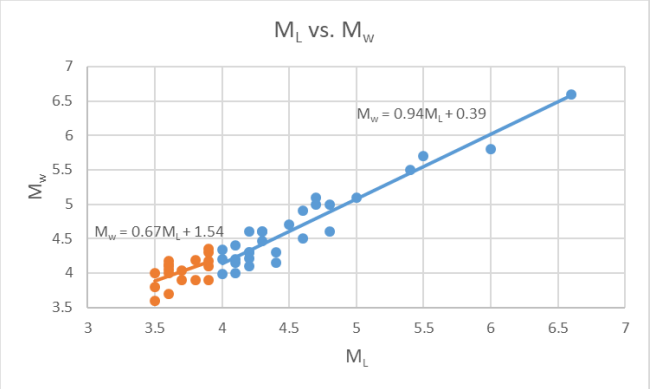

Figure 3 M_L vs. M_W comparison for the earthquakes used in this study. Solid lines represent the trend lines. Orange color $M_L < 4.0$ and the blue color $M_L \geq 4.0$.

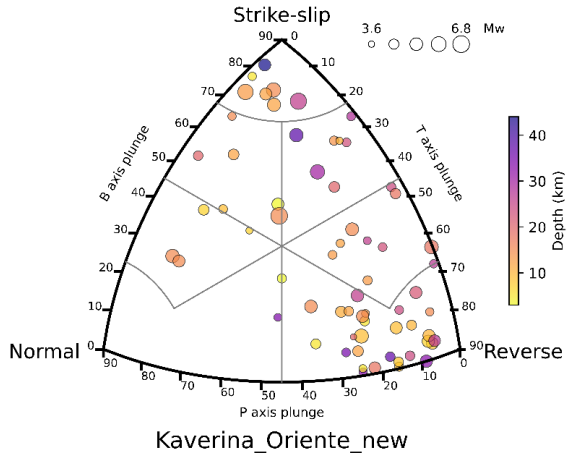

Figure 4 Distribution diagram of double couple focal mechanism, according to the standard classification (Kaverina et al., 1996). The diagram includes the 65 earthquakes of this study.

ing of recent sediments in the eastern half of the Oriente Deep Zone (Calais et al., 1998; Calais and de Lepinay, 1991), but likely involves the entire southeastern Cuban margin and the Oriente fault itself within the longitude range of the Oriente Deep Zone.

3.3 Santiago Deformed Belt

In the 76.25°W to ~75°W longitude range, the Santiago Deformed Belt (Figure 2c) is the most seismically active segment of the southeastern Cuban margin (Álvarez et al., 1999). It hosts approximately 45% of the moment tensor solutions determined here as well as from the gCMT database (1c-4c, 1, 3-8, 10-12, 18, 20-26, 1*, 2* 4*, 6*, 10*, 11*, and 13*). A detailed study of the detection level of the SSNC shows that this majority is not an artifact of the geometry of the observational network (Diez Zaldivar et al., 2022). Reverse faulting dominates the dataset, being observed in 22 of 28 earthquakes (79%), particularly in association with the 2016 seismic swarm near 76°W, with N-S trending fault planes (González et al., 2021). In the central part of the SDB, earthquake fault planes (10, 11, 12, 18, 22, 10*, 11*, and 13*) closer to E-W and reverse and reverse-oblique faulting with dip angle ranging from 50° to 70° is predominant. The inversion of focal mechanisms for a stress tensor is consistent with a thrust faulting regime (Figure 5c). This is consistent with the geological mapping of folds and reverse faults, which result in the south-verging thrusting of a narrow sliver of crust of the southeastern Cuba margin over the Gonâve microplate (Calais and de Lepinay, 1990, 1991).

A N-S profile of earthquakes located by more than 4 stations with an rms < 0.5 s (Figure 6), shows the occurrence of events (e.g. 11, 12, 10*, 11*, and 13*) well below the Moho, whose depth is ~17 km (González et al., 2012), in this transform system, while focal mechanisms indicate that several north-dipping reverse faults may be involved in the compressional sliver of the Santiago Deformed Belt, as also observed in the marine geophysical data (Calais et al., 1998). This sliver is bounded to the north by the Oriente fault itself, whose dip angle is not well-determined, but likely close to vertical. Interestingly, GNSS measurements inland in eastern Cuba show no evidence for N-S shortening, only left-lateral shear parallel to the direction of the Oriente fault (Calais et al., 2023).

3.4 The South and Southeast of Guantanamo

East of the main earthquake cluster of the Santiago Deformed Belt (Figure 2a), events 5c, 8c, 11c, 2, and 13 still exhibit a combination of strike-slip and reverse faulting, probably associated to the reverse faulting observed along the eastern end of the Santiago Deformed Belt (Calais et al., 1998) or its possible continuation across the Windward Passage along compressional offshore structures mapped to the south of the Northwest Peninsula of Haiti (Corbeau et al., 2019). The stress regime inferred from focal mechanisms in this area is consistent with a combination of thrust faulting with a significant strike-slip component (Figure 5d).

3.5 Overall stress regime along the southeastern Cuban margin

We used all moment tensor solutions determined here along the southern margin of eastern Cuba, together with 16 additional ones from the gCMT database, to compute a regional stress tensor and determine the consistency of the focal solutions with a single regime for that segment of the Oriente fault. The variety of focal mechanisms types observed here along the southeastern Cuban margin is indeed intriguing, though similar variability is observed along other transform faults boundaries such as the northern margin of the Scotia plate (Giner-Robles et al., 2003), the southern region of the San Andreas fault system (Mount and Suppe, 1987), or the Dead Sea transform fault (Garfunkel et al., 1981). Despite the variety of focal mechanisms, the overall stress inversion indicates a thrust regime with well-defined orientations of the three principal stress axes.

The inversion results, displayed in Figure 7a, show σ_3 close to vertical with a plunge angle between 60° and

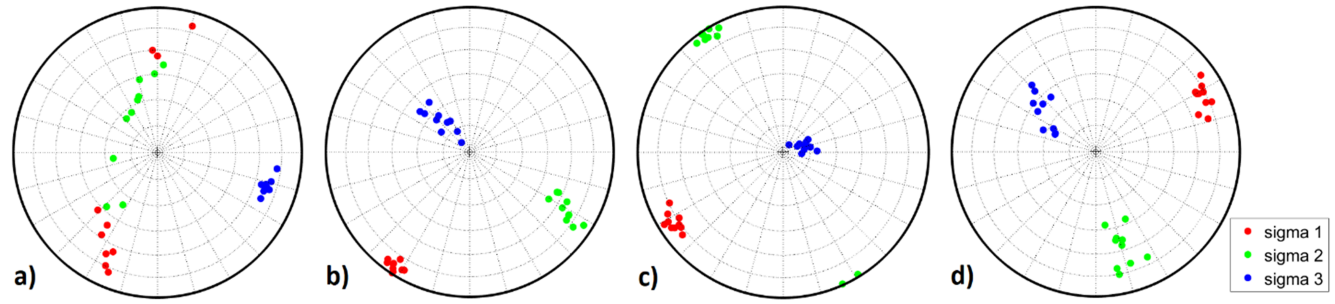

	Cabo Cruz Basin			Oriente Deep Zone			Santiago Deformed Belt			South of Guantánamo		
	sigma 1	sigma 2	sigma 3	sigma 1	sigma 2	sigma 3	sigma 1	sigma 2	sigma 3	sigma 1	sigma 2	sigma 3
Azimuth	200±35	302±65	108±8	212±5.8	120±7.8	311±23.6	237±8.5	328±7.9	67±29.1	63±8.3	165±12.6	305±30
Plunge	4.7±18	69±16	21±3.8	4.6±2.7	27±10.3	62±10	15±2.9	2.6±3.0	74±2.8	20±4.7	31±12.5	52±10.4

Figure 5 Confidence limits of the principal stress axes direction estimated by the stress tensor inversion using the STRESSINVERSE codes (Vavryčuk, 2014) for each zone: a) Cabo Cruz Bazin; b) Oriente Deep Zone; c) Santiago Deformed Belt; and d) Southeast of Guantanamo province.

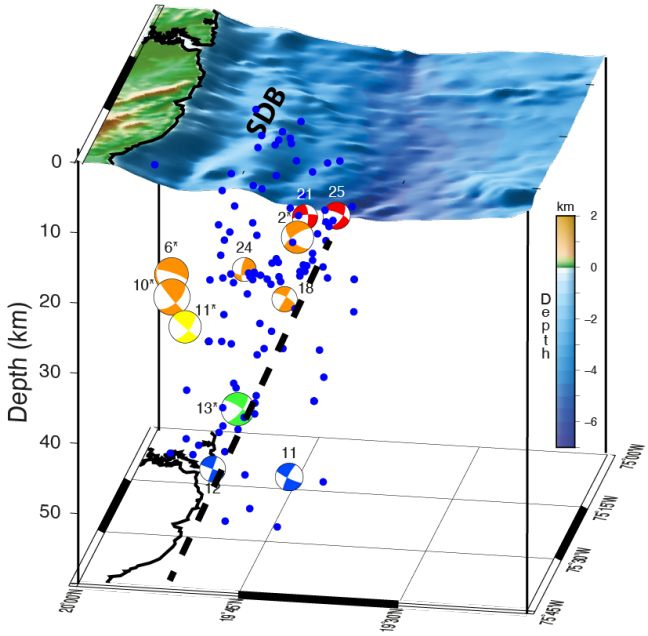

Figure 6 North-South seismicity profile (blue circles) using earthquakes with M > 3, registered by more than 4 digital stations, located with rms < 0.5 s, and in longitude range from 75.75°W to 75.00°W (eastern part of the Santiago Deformed Belt, see fig. 2c) during the study period from 01/01/2015 to 30/11/2024. Black dashed line represents the possible South-North dipping of the fault zone. The beachballs are color-coded by depth, scaled by magnitude, and rotated to illustrate the viewing angle.

85°, while σ_1 is close to horizontal, with a plunge angle between 5° and 10° and an azimuth of ~220° (i.e., NE-SW). This, together with a shape ratio of 0.85±5, is indicative of a stress regime close to pure compression, with a most compressional stress direction (σ_1) oblique to the east-west direction of the Oriente transform fault. Though classical faulting theory predicts that maximum compressional stress should lie horizontally at 30° to 45° from the strike of vertical strike-slip faults (e.g., Anderson, 1951), that the minimum compressional stress (σ_3) stress is vertical, or close to it, is uncommon in such a context. There is little doubt from GNSS geodesy that the Gonâve-North America relative motion is parallel to the strike of the Oriente fault along the entire length of the Cayman trough, with no significant convergence component at the longitude of Cuba (Symithe et al., 2015; Calais et al., 2023), contrary to early hypotheses that sought to explain the compressional Santiago Deformed Belt (e.g., Calais et al., 1998). In addition, the geometry of the Oriente fault off southeastern Cuba is not that of a restraining bend as observed, for instance, in the case of the Transverse Ranges of Southern California along the San Andreas fault (e.g., Luyendyk, 1991), or in the Lebanon restraining bend along the Dead Sea fault (e.g., Gomez et al., 2006). The trace of the Oriente fault offshore Cuba is rather a series of left-stepping, hence transtensional, segments separated by small pull-apart basins (Figure 1; Calais and de Lepinay, 1991).

Therefore, other effects must be invoked to explain a stress regime close to purely compressional along the Oriente fault offshore Cuba, perhaps the stresses induced by the horizontal gradients in gravitational potential energy between southeastern Cuba, which culminates at 1300 m in the Sierra Maestra, and the >-7000 m-deep offshore bathymetry, two contrasting reliefs within only a few tens of kilometers of each other. The active role of the sublithospheric mantle, the effect of fluid pore pressure on effective fault friction, or local block rotations may also be invoked. Further data and analysis is required to confirm and fully understand this peculiarity of the Oriente fault off southeastern Cuba.

4 Conclusions

Using the records from the broadband seismic network operating in Cuba and the surrounding countries, we determined a set of 49 deviatoric moment tensor solutions through full waveform inversion for earthquakes with M ≥ 3.5, from 2015 to the end of 2024, along the Oriente fault system, off southeastern Cuba. We compare 14 of these events with independently determined solutions and find results similar to the ones we determined,

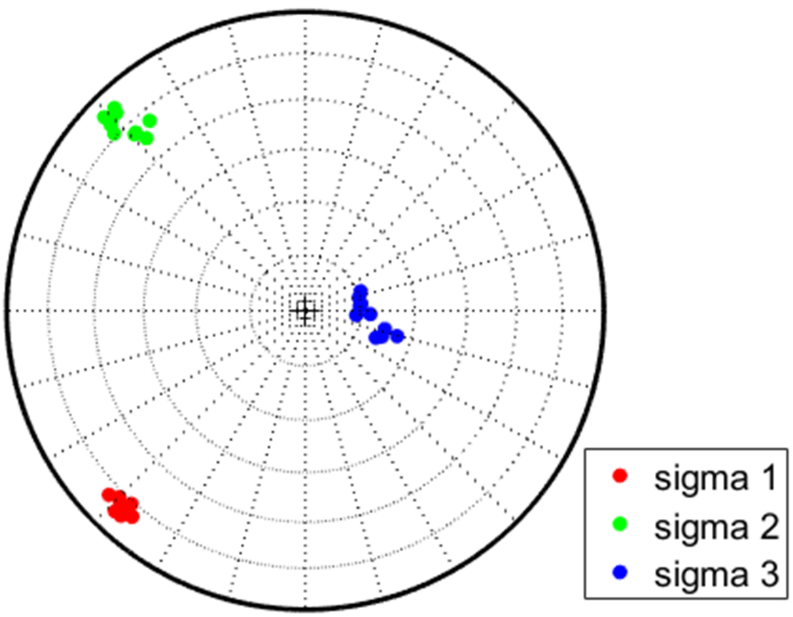

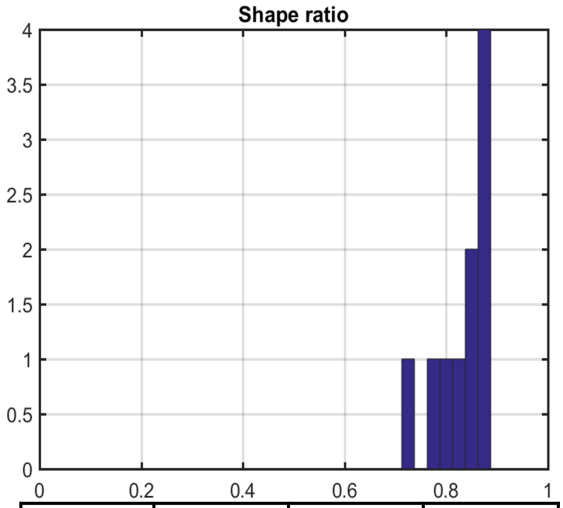

	sigma 1	sigma 2	sigma 3
Azimuth	222±4.2	316±5.5	109±31
Plunge	9.8±2.1	22±7	66±5.7

Figure 7 a) Confidence limits of the principal stress axes direction for all the focal mechanism in the region; b) The corresponding stress shape ratio. The table shows the best-fitting values.

which validates our approach. A comparison between the moment magnitudes determined here and the local magnitude routinely calculated by the Cuban National Seismological Service shows a good agreement for Mw > 4, consistent with Kanamori (1983). For Mw < 4, we find the relationship Mw ≈ (2/3)M_L, similar to that observed in other regions, for instance the Lesser Antilles (González et al., 2017).

The moment tensor solutions calculated here, together with 16 additional ones from the gCMT database, highlight the along-strike segmentation of the Oriente fault system, inferred so far from marine geophysical data only. We find oblique normal faulting in the Cabo Cruz transtensional step-over, and oblique reverse faulting further east in the Oriente Deep Zone and the transpressional Santiago Deformed Belt, which concentrates most of the seismicity studied here. The Oriente fault, though largely strike-slip, may have a small reverse component itself, as exemplified by the November 10, 2024, Mw 6.8 earthquake. The bulk of reverse/oblique faulting earthquakes, however, coincide with the Santiago Deformed Belt, a narrow crustal sliver overthrusting to the south the extended island arc crust of the eastern Cayman Trough and likely bounded to the north by the Oriente fault.

Several intriguing features also emerge, to be investigated in future research, in particular the occurrence of earthquakes well below the Moho in this transform system and the wide variety of fault plane directions in particular in the Santiago Deformed Belt.

Acknowledgements

The authors are grateful to the National Seismological Service of the National Centre for Seismological Research of Cuba and the NSF SAGE data archive operated by EarthScope Consortium (NSF award 1724509), which provided the data used in this study. We thank the staff of the Laboratory Géosciences Environnement Toulouse (GET), member of the Observatoire Midi-Pyrénées (OMP) of the University of Toulouse III Paul Sabatier, and the Observatoire Volcanologique et Sismologique de la Martinique (OVSM) of the Institut de Physique du Globe de Paris (IPGP), for their support and facilities for the research team. We acknowledge funding from the FEDER European Community program through the Interreg Caraïbes "PREST" project, grant number 5236, from the French National Research Agency, "CAST project", grant number ANR-22-CE01-0019, and from the "DISA-Desarrollo de Investigaciones Sismológicas Aplicadas en la República de Cuba" program, through "Analysis of the structure and dynamics of the crust in the arc of the Antilles" and "Generación de sismogramas sintéticos para Santiago de Cuba", projects codes PS211SC001-027 and PS211SC001-040.

The authors express their sincere thanks to the anonymous reviewers and the editors, particularly Robert Skoumal, for their rigorous review and helpful recommendations, which strengthened the manuscript.

Event #	Origin time yyyymmdd hh:mm:ss.ss	Lat Lon Depth (hypocentr) (centroid)	min - max Δ (km)	MLv	Mw	Strike Dip Rake NP1 / NP2	Moment Tensor (deviatoric)	DC %	VR %	NC	SNR	CN
1	20150313 17:24:26.50	19.95 -75.912 22.6 19.8958 -75.8834 24	23-256	3.9	4.3	167 58 93 342 32 86	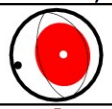	31.5	50	13	11	2.3
2	20150323 06:11:31.80	19.231 -73.697 8 19.3394 -73.6113 20	119-255	4.2	4.3	251 62 -156 149 69 -30	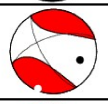	42.1	52	12	4	2.0
3	20150728 00:50:44.10	19.852 -76.057 11.5 19.8791 -76.0284 12	41-238	3.6	4.05	216 75 126 326 39 25	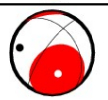	19.4	57	16	7	2.7
4	20151013 07:07:25.70	19.849 -75.904 11.1 20.0387 -75.9613 24	27-294	4.0	4.2	203 57 146 313 62 38	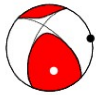	82.5	55	25	19	4.4
5	20160118 06:16:37.60	19.788 -76.047 5 19.8151 -76.0756 3	44-508	3.9	4.35	220 69 105 3 25 55		53.8	65	22	26	3.4
6	20160121 20:12:35.40	19.758 -76.082 3 19.758 -76.0534 4	42-228	4.4	4.15	311 75 -45 55 47 -160	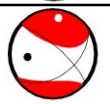	33.7	45	18	19	1.4
7	20160125 22:37:10.00	19.696 -76.103 5 19.7231 -76.103 5	45-512	4.3	4.47	15 13 139 145 82 80		67.7	58	22	96	3.5
8	20160126 10:59:24.20	19.706 -76.099 5 19.6789 -76.0704 10	45-215	4.1	4.4	155 57 78 356 35 107	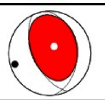	72.1	72	18	39	2.5
9	20160328 13:57:32.50	19.827 -73.868 10 19.9625 -73.9253 23	54-425	4.2	4.1	59 64 55 297 43 139	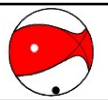	79.2	68	19	8	3.2
10	20160914 22:24:35.70	19.723 -75.647 15.7 19.8314 -75.733 27	41-165	3.7	4.04	102 48 59 324 51 119	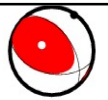	78.5	63	18	17	3.2
11	20170425 14:42:59.70	19.682 -75.471 42.1 19.682 -75.4424 37	57-446	4.4	4.3	79 63 94 249 28 82	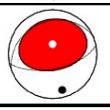	58.8	61	22	11	2.0

Table 2 Continued on next page

12	20170803 18:58:24.40	19.798 -75.46 41 19.8522 -75.4886 33	51-447	4.0	3.99	90 70 91 265 21 86	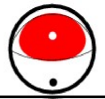	65	42	22	5	3.2
13	20200124 02:47:00.20	19.797 -74.735 16.2 19.797 -74.7636 14	42-337	4.2	4.21	270 77 27 173 64 165	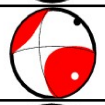	56.3	80	27	11	2.7
14	20200517 22:41:23.20	19.745 -76.464 5 19.7179 -76.5212 13	26-239	3.8	4.19	132 68 116 261 33 44	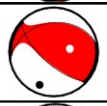	85.6	80	24	16	3.6
15	20200517 23:00:21.70	19.738 -76.465 5 19.738 -76.5222 13	27-239	3.6	4.12	145 77 123 253 35 22	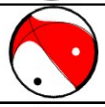	75	65	27	14	3.7
16	20200518 07:18:06.70	19.699 -76.453 3.4 19.7261 -76.4816 12	31-548	4.0	4.34	129 73 108 262 24 46	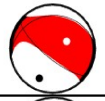	69.6	82	30	23	3.6
17	20210530 08:29:48.40	19.468 -78.064 10 19.5493 -78.0926 3	180-409	3.6	4.18	144 27 -180 54 90 -63		30.9	47	19	9	4.4
18	20210719 01:33:26.60	19.689 -75.494 18.3 19.7974 -75.5513 24	91-449	3.9	4.18	92 60 73 304 34 117	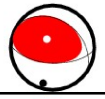	80.6	67	26	10	1.7
19	20210926 11:41:21.80	19.847 -76.485 13.6 19.8741 -76.485 35	16-343	4.1	4.15	124 74 83 327 17 113		33.5	70	26	5	2.4
20	20210926 15:15:23.40	19.85 -75.933 14.8 19.9042 -75.9617 15	52-246	3.5	4.0	31 70 -167 297 78 -20	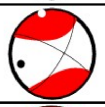	37	53	17	5	2.1
21	20230808 02:26:15.90	19.658 -75.54 7.3 19.793 -75.54 34	41-263	3.8	3.9	291 89 -73 24 17 -177		92.4	59	19	4	2.1
22	20240323 15:46:49.7	19.72 -75.38 20 19.91 -75.38 20	36-281	3.5	3.6	81 72 79 294 21 121	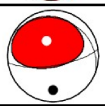	63	56	15	3	3.4
23	20240610 14:55:02.6	19.90 -75.853 26.2 19.878 -75.824 15	13-248	4.1	4.0	179 52 105 336 41 72	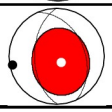	34.6	76	18	24	5.7

Table 2 Continued on next page

24	20240816 23:18:46.7	19.75 -75.52 14.3 19.696 -75.491 7	47-271	3.6	3.7	172 40 -167 72 82 -51	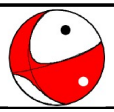	81	53	15	7	2.1
25	20240907 23:09:56.8	19.61 -75.57 7.1 19.61 -75.54 9	55-260	4.1	4.2	311 29 91 129 61 89		75	52	18	11	1.7
26	20241017 14:50:32.5	19.73 -76.001 12.6 19.726 -75.921 20	96-545	4.3	4.6	261 52 17 161 77 141	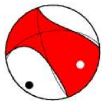	47	54	30	29	2.3
27	20241110 18:45:36.0	19.71 -77.08 10 19.71 -77.156 18	128-244	4.6	4.5	163 56 144 274 61 39	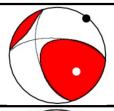	74	55	18	7	3.6
28	20241110 21:27:53.0	19.73 -77.168 10 19.757 -77.197 23	136-252	3.9	4.1	258 64 18 160 74 152	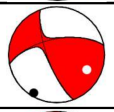	94	71	18	4	3.3
29	20241111 18:11:51.0	19.93 -77.25 15 19.822 -77.193 28	141-257	3.6	4.1	6 71 162 102 73 20	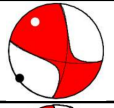	82	52	21	5	3.1
30	20241113 03:36:50.0	19.74 -77.05 10 19.713 -77.107 10	124-240	3.5	3.8	94 64 16 357 75 153	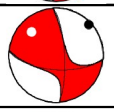	78	54	21	2	3.1
31	20241119 11:13:33.0	19.77 -77.2 10 19.743 -77.257 26	159-254	3.7	3.9	159 42 146 275 68 53	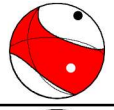	31	50	17	4	3.1
32	20241120 07:22:06.0	19.75 -76.99 10 19.75 -77.047 5	138-233	3.9	3.9	112 70 92 285 20 84	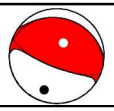	88	60	18	3	2.9
33	20241121 13:17:19.0	19.765 -77.194 10 19.711 -77.194 5	159-254	3.6	4.0	179 83 -170 88 80 -7	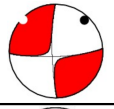	92	70	18	5	3.0
34	20241125 06:52:48.0	19.69 -77.03 5 19.744 -77.03 8	144-239	4.2	4.3	104 61 88 289 29 94	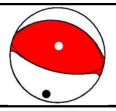	93	82	15	6	3.9
35	20241213 14:04:33.0	19.82 -76.94 8.8 19.793 -77.026 13	142-231	4.1	3.9	46 69 73 267 27 127	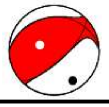	82	65	14	7	2.5

Table 2 New focal mechanisms derived in this study (Set 2). min - max Δ are the hypocentral distance of the nearest and farthest station used for the inversion; NC is the number of components used; SNR the signal to noise ratio; K is the mean Kagan angle of the family of the acceptable solutions and CN is the condition number. For the remaining symbols, see legend of Table 1.

Data and Code Availability

Earthquake parameters used in this study were obtained from the SSNC catalog (https://www.cenais.gob.cu/navegador/). Seismic waveform data were downloaded from the IRIS DMC repository (https://ds.iris.edu/wilber3/find_event), using instrument response information from both the IRIS Data Center (https://ds.iris.edu/SeismiQuery/responses.htm) and the SISMOB mobile network managed by Epos-France (https://seismology.resif.fr/).

Signal preprocessing was performed using the SAC software package (https://ds.iris.edu/ds/nodes/dmc/software/downloads/sac), and moment tensor solutions were computed with the ISOLA software (https://geo.mff.cuni.cz/~ jz/for_ISOLAnews/). Regional stress inversion was calculated using the STRESSINVERSE code (https://www.ig.cas.cz/stress-inverse/).

Focal mechanism distributions were plotted using the FMC tool (https://github.com/Jose-Alvarez/FMC). Maps and figures were generated in part using the Generic Mapping Tools (GMT, https://www.generic-mapping-tools.org).

Competing Interests

The authors declare that they have no known competing financial interests or personal relationships that could have appeared to influence the work reported in this publication

References

Álvarez, J., Chuy, T., García, J., Moreno, B., Álvarez, H., Blanco, M., Expósito, O., González, O., and Fernández, A. An earthquake catalogue of Cuba and neighboring areas. In *Internal report of the Abdus Salam International Centre for Theoretical Physics. IC/IR/99/1 (ICTP)*. 1999.

Álvarez, L., Rubio, M., Chuy, T., and Cotilla, M. Estudio de la sismicidad de la región del Caribe y estimación preliminar de la peligrosidad sísmica en Cuba. Informe final del tema 310.01. *Inst. de Geofísica y Astronomía*, 1985.

Álvarez Gómez, J. A. FMC—Earthquake focal mechanisms data management, cluster and classification. *SoftwareX*, 9:299–307, Jan. 2019. doi: 10.1016/j.softx.2019.03.008.

Anderson, E. *The Dynamics of Faulting and Dyke Formation*. Oliver and Boyd, Edinburgh, 1951.

Benford, B., DeMets, C., and Calais, E. GPS estimates of microplate motions, northern Caribbean: Evidence for a Hispaniola microplate and implications for earthquake hazard. *Geophysical Journal International*, 191(2), 2012. doi: 10.1111/j.1365-246x.2012.05662.x.

Burke, K. Tectonic Evolution of the Caribbean. *Annual Review of Earth and Planetary Sciences*, 16(1):201–230, May 1988. doi: 10.1146/annurev.ea.16.050188.001221.

Calais, E. and de Lepinay, B. M. A Natural Model of Active Transpressional Tectonics the en Échelon Structures of the Oriente Deep, Along the Northern Caribbean Transcurrent Plate Boundary (Southern Cuban Margin). *Revue de l'Institut Français du Pétrole*, 45(2):147–160, Mar. 1990. doi: 10.2516/ogst:1990013.

Calais, E. and de Lepinay, B. M. From transtension to transpression along the northern Caribbean plate boundary off Cuba: implications for the Recent motion of the Caribbean plate. *Tectonophysics*, 186(3-4):329–350, Feb. 1991. doi: 10.1016/0040-1951(91)90367-2.

Calais, E., Perrot, J., and de Lépinay, B. M. *Strike-slip tectonics and seismicity along the northern Caribbean plate boundary from Cuba to Hispaniola*. Geological Society of America, 1998. doi: 10.1130/0-8137-2326-4.125.

Calais, E., Gonzalez, O., Arango-Arias, E., Moreno, B., Palau, R., Cutie, M., Diez, E., Montenegro, C., Rodriguez Roche, E., Garcia, J., Castellanos, E., and Symithe, S. Current deformation along the northern Caribbean plate boundary from GNSS measurements in Cuba. *Tectonophysics*, 868:230068, Dec. 2023. doi: 10.1016/j.tecto.2023.230068.

Calais, E., Delouis, B., Ampuero, J.-P., Bao, H., Courboulex, F., Deschamps, A., De Lépinay, B., Monfret, T., Meng, L., Xu, L., DeMets, C., Gonzalez, O., Arango-Arias, E., Moreno, B., Palau, R., Cutie, M., Diez, E., Roche, E., Garcia, J., Castellanos, E., Symithe, S., and Williams, P. The 28 January 2020, Mw7.7, Cayman Trough / Oriente Fault, Supershear Earthquake Rupture. *Seismica*, 4(2), Aug. 2025. doi: 10.26443/seismica.v4i2.1629.

Clouard, V. PREST in Cuba temporary experiment installed in the southeast of Cuba for better understand the dynamics of the lithosphere at the plate boundary, Cuba (RESIF-SISMOB), 2018. doi: 10.15778/RESIF.XH2018.

Corbeau, J., Gonzalez, O., Clouard, V., Rolandone, F., Leroy, S., Keir, D., Stuart, G., Momplaisir, R., Boisson, D., and Prépetit, C. Is the local seismicity in western Hispaniola (Haiti) capable of imaging northern Caribbean subduction? *Geosphere*, 15(6), 2019. doi: 10.1130/ges02083.1.

Cotilla Rodriguez, M., Franzke, H., and Cordoba Barba, D. Seismicity and seismoactive faults of Cuba. *Russian Geology and Geophysics*, 48(6), 2007. doi: 10.1016/j.rgg.2006.08.004.

DeMets, C., Jansma, P. E., Mattioli, G. S., Dixon, T. H., Farina, F., Bilham, R., Calais, E., and Mann, P. GPS geodetic constraints on Caribbean-North America Plate Motion. *Geophysical Research Letters*, 27(3):437–440, Feb. 2000. doi: 10.1029/1999gl005436.

Di Giacomo, D., Harris, J., and Storchak, D. A. Complementing regional moment magnitudes to GCMT: a perspective from the rebuilt International Seismological Centre Bulletin. *Earth System Science Data*, 13(5):1957–1985, May 2021. doi: 10.5194/essd-13-1957-2021.

Diez Zaldivar, E. R., Priolo, E., Sandron, D., Poveda Brossard, V., Cattaneo, M., Marzorati, S., and Palau Clares, R. Evaluation of the Event Detection Level of the Cuban Seismic Network. *Seismological Research Letters*, 93(4), 2022. doi: 10.1785/0220220016.

Dorel, J. *et structure de l'arc des Petites Antilles et du bassin Atlantique*. PhD thesis, Université Pierre et Marie Curie, 1978.

Dreger, D. S. *Time-Domain Moment Tensor INVerse Code (TDMT_INVC) Version 1.1, Berkeley Seismological Laboratory*, page 1627. Elsevier, 2003. doi: 10.1016/s0074-6142(03)80290-5.

Dziewonski, A. M., Chou, T., and Woodhouse, J. H. Determination of earthquake source parameters from waveform data for studies of global and regional seismicity. *Journal of Geophysical Research: Solid Earth*, 86(B4):2825–2852, Apr. 1981. doi: 10.1029/jb086ib04p02825.

Ekström, G., Nettles, M., and Dziewoński, A. The global CMT project 2004–2010: Centroid-moment tensors for 13,017 earthquakes. *Physics of the Earth and Planetary Interiors*, 200-201, 2012. doi: 10.1016/j.pepi.2012.04.002.

García, J., Slejko, D., Alvarez, L., Peruzza, L., and Rebez, A. Seismic Hazard Maps for Cuba and Surrounding Areas. *Bulletin of the Seismological Society of America*, 93(6):2563–2590, Dec. 2003. doi: 10.1785/0120020144.

García-Casco, A., Iturralde-Vinent, M. A., and Pindell, J. Latest Cretaceous Collision/Accretion between the Caribbean Plate and Caribeana: Origin of Metamorphic Terranes in the Greater Antilles. *International Geology Review*, 50(9), 2008. doi: 10.2747/0020-6814.50.9.781.

Garfunkel, Z., Zak, I., and Freund, R. Active faulting in the dead sea rift. *Tectonophysics*, 80(1-4):1–26, Dec. 1981. doi: 10.1016/0040-1951(81)90139-6.

Giner-Robles, J., González-Casado, J., Gumiel, P., Martín-Velázquez, S., and García-Cuevas, C. A kinematic model of the Scotia plate (SW Atlantic Ocean). *Journal of South American Earth Sciences*, 16(4):179–191, Aug. 2003. doi: 10.1016/s0895-9811(03)00064-6.

Goldstein, P. *SAC User's Manual*. Lawrence Livermore Laboratory, University of California, 1999.

Gomez, F., Khawlie, M., Tabet, C., Nasser Darkal, A., Khair, K., and Barazangi, M. Late Cenozoic uplift along the northern Dead Sea transform in Lebanon and Syria. *Earth and Planetary Science Letters*, 241(3-4):913–931, Jan. 2006. doi: 10.1016/j.epsl.2005.10.029.

González, O., Moreno, B., Romanelli, F., and Panza, G. F. Lithospheric structure below seismic stations in Cuba from the joint inversion of Rayleigh surface-waves dispersion and receiver functions. *Geophysical Journal International*, 189(2):1047–1059, Mar. 2012. doi: 10.1111/j.1365-246x.2012.05410.x.

González, O., Arango, E., and Leyva, M. Tensor del momento sísmico mediante inversión de ondas del terremoto principal de la actividad sísmica de enero y febrero del 2014 en la región noroeste de Villa Clara, Cuba. *Anuario de la Sociedad Cubana de Geología*, (3), 2015.

González, O., Clouard, V., and Zahradnik, J. Moment tensor solutions along the central Lesser Antilles using regional broadband stations. *Tectonophysics*, 717:214–225, Oct. 2017. doi: 10.1016/j.tecto.2017.06.024.

González, O., Arango, E., Moreno, B., Leyva, M., and Berenguer, Y. Comportamiento de la actividad sísmica anómala iniciada el 17 de enero de 2016 al sur de Santiago de Cuba. *Revista de Minería y Geología*, 37, 2021.

González, O. F., Alvarez, J. L., Moreno, B., and Panza, G. F. S-Wave Velocities of the Lithosphere–Asthenosphere System in the Caribbean Region. *Pure and Applied Geophysics*, 169(1-2), 2011. doi: 10.1007/s00024-011-0321-3.

Graves, R. and Pitarka, A. Broadband time history simulation using a hybrid approach. In *Proc. 13th World Conf. Earthquake Eng*, Vancouver, Canada, 2004. paper no. 1098.

Havskov, J. and Ottemöller, L. *Routine Data Processing in Earthquake Seismology*, page 101–149. Springer Netherlands, 2010. doi: 10.1007/978-90-481-8697-6_5.

Iturralde-Vinent, M. Geología de las ofiolitas de Cuba. *Special Contribution*, n.1:83–120, 1996.

Iturralde-Vinent, M., García-Casco, A., Rojas-Agramonte, Y., Proenza, J., Murphy, J., and Stern, R. The geology of Cuba: A brief overview and synthesis. *GSA Today*, 2016. doi: 10.1130/gsatg296a.1.

Kagan, Y. Y. 3-D rotation of double-couple earthquake sources. *Geophysical Journal International*, 106(3), 1991. doi: 10.1111/j.1365-246x.1991.tb06343.x.

Kanamori, H. Magnitude scale and quantification of earthquakes. *Tectonophysics*, 93(3-4):185–199, Apr. 1983. doi: 10.1016/0040-1951(83)90273-1.

Kaverina, A. N., Lander, A. V., and Prozorov, A. G. Global Creepex Distribution and Its Relation to Earthquake-Source Geometry and Tectonic Origin. *Geophysical Journal International*, 125(1): 249–265, Apr. 1996. doi: 10.1111/j.1365-246x.1996.tb06549.x.

Konstantinou, K. I. and Rontogianni, S. A Comparison of Teleseismic and Regional Seismic Moment Estimates in the European-Mediterranean Region. *Seismological Research Letters*, 82(2): 188–200, Mar. 2011. doi: 10.1785/gssrl.82.2.188.

Krizova, D., Zahradnik, J., and Kiratzi, A. Resolvability of Isotropic Component in Regional Seismic Moment Tensor Inversion. *Bulletin of the Seismological Society of America*, 103(4), 2013. doi: 10.1785/0120120097.

Kumar, R., Gupta, S., and Kumar, A. Non-double-couple mechanism of moderate earthquakes occurred in Lower Siang region of Arunachal Himalaya: Evidence of factors affecting non-DC. *Journal of Asian Earth Sciences*, 98:105–115, Feb. 2015. doi: 10.1016/j.jseaes.2014.10.025.

Leroy, S., Mauffret, A., Patriat, P., and Mercier de Lepinay, B. An alternative interpretation of the Cayman trough evolution from a reidentification of magnetic anomalies. *Geophysical Journal International*, 141(3), 2000. doi: 10.1046/j.1365-246x.2000.00059.x.

Luyendyk, B. P. A model for Neogene crustal rotations, transtension, and transpression in southern California. *Geological Society of America Bulletin*, 103(11):1528, 1991. doi: 10.1130/0016-7606(1991)103<1528:amfncr>2.3.co;2.

Mann, P. and Burke, K. Neotectonics of the Caribbean. *Reviews of Geophysics*, 22(4):309–362, Nov. 1984. doi: 10.1029/rg022i004p00309.

Mann, P., Taylor, F., Edwards, R., and Ku, T.-L. Actively evolving microplate formation by oblique collision and sideways motion along strike-slip faults: An example from the northeastern Caribbean plate margin. *Tectonophysics*, 246(1-3), 1995. doi: 10.1016/0040-1951(94)00268-e.

Moreno, B., Grandison, M., and Atakan, K. Crustal velocity model along the southern Cuban margin: implications for the tectonic regime at an active plate boundary. *Geophysical Journal International*, 151(2):632–645, Nov. 2002. doi: 10.1046/j.1365-246x.2002.01810.x.

Mount, V. S. and Suppe, J. State of stress near the San Andreas fault: Implications for wrench tectonics. *Geology*, 15(12):1143, 1987. doi: 10.1130/0091-7613(1987)15<1143:sosnts>2.0.co;2.

Munafò, I., Malagnini, L., and Chiaraluce, L. On the Relationship between Mw and ML for Small Earthquakes. *Bulletin of the Seismological Society of America*, 106(5), 2016. doi: 10.1785/0120160130.

Nafe, J. and Drake, C. Physical properties of marine sediments. In M.N.Hill, W.-I. and NewYork, editors, *The Sea*, volume 3, page 794–815. 1960.

Patton, H. J. and Randall, G. E. On the causes of biased estimates of seismic moment for earthquakes in central Asia. *Journal of Geophysical Research: Solid Earth*, 107(B11), Nov. 2002. doi: 10.1029/2001jb000351.

Perrot, J., Calais, E., and Mercier de Lépinay, B. Tectonic and Kinematic Regime along the Northern Caribbean Plate Boundary: New Insights from Broad-band Modeling of the May 25, 1992, Ms = 6.9 Cabo Cruz, Cuba, Earthquake. *Pure and Applied Geophysics*, 149(3), 1997. doi: 10.1007/s000240050036.

Rösler, B., Stein, S., Ringler, A., and Vackář, J. Apparent Non-Double-Couple Components as Artifacts of Moment Tensor Inversion. *Seismica*, 3(1), Apr. 2024. doi: 10.26443/seismica.v3i1.1157.

Sokos, E. and Zahradnik, J. Evaluating Centroid-Moment-Tensor Uncertainty in the New Version of ISOLA Software. *Seismological Research Letters*, 84(4), 2013. doi: 10.1785/0220130002.

Sokos, E. N. and Zahradnik, J. ISOLA a Fortran code and a Mat-

lab GUI to perform multiple-point source inversion of seismic data. *Computers & Geosciences*, 34(8):967–977, Aug. 2008. doi: 10.1016/j.cageo.2007.07.005.

Sylvester, A. G. Strike-slip faults. *Geological Society of America Bulletin*, 100(11):1666–1703, Nov. 1988. doi: 10.1130/0016-7606(1988)100<1666:ssf>2.3.co;2.

Symithe, S., Calais, E., de Chabalier, J. B., Robertson, R., and Higgins, M. Current block motions and strain accumulation on active faults in the Caribbean. *Journal of Geophysical Research: Solid Earth*, 120(5):3748–3774, May 2015. doi: 10.1002/2014jb011779.

Vacka , J., Burjanek, J., and Zahradnik, J. Automated Detection of Long-Period Disturbances in Seismic Records; MouseTrap Code. *Seismological Research Letters*, 86(2A):442–450, Jan. 2015. doi: 10.1785/0220140168.

van der Elst, N. J. and Shaw, B. E. Larger aftershocks happen farther away: Nonseparability of magnitude and spatial distributions of aftershocks. *Geophysical Research Letters*, 42(14), 2015. doi: 10.1002/2015gl064734.

Van Dusen, S. R. and Doser, D. I. Faulting Processes of Historic (1917–1962) M≥ 6.0 Earthquakes Along the North-central Caribbean Margin. *Pure and Applied Geophysics*, 157(5): 719–736, May 2000. doi: 10.1007/pl00001115.

Vavryčuk, V. Non-double-couple earthquakes of 1997 January in West Bohemia, Czech Republic: evidence of tensile faulting. *Geophysical Journal International*, 149(2):364–373, May 2002. doi: 10.1046/j.1365-246x.2002.01654.x.

Vavryčuk, V. Iterative joint inversion for stress and fault orientations from focal mechanisms. *Geophysical Journal International*, 199(1), 2014. doi: 10.1093/gji/ggu224.

Vega-Garriga, N., Cuevas-Ojeda, J., Arango-Arias, E., Alcaide-Orpi, J., and Ríos-Martínez, Y. Evaluación de las causas de la sismicidad originada en las provincias centrales de Cuba. *Minería y Geología*, 38:24–38, 2022.

Yue, H. and Lay, T. Resolving Complicated Faulting Process Using Multi-Point-Source Representation: Iterative Inversion Algorithm Improvement and Application to Recent Complex Earthquakes. *Journal of Geophysical Research: Solid Earth*, 125(2), Jan. 2020. doi: 10.1029/2019jb018601.

Zahradnik, J. and Plesinger, A. Toward Understanding Subtle Instrumentation Effects Associated with Weak Seismic Events in the Near Field. *Bulletin of the Seismological Society of America*, 100(1):59–73, Jan. 2010. doi: 10.1785/0120090087.

Zahradník, J. and Plešinger, A. Long-Period Pulses in Broadband Records of Near Earthquakes. *Bulletin of the Seismological Society of America*, 95(5):1928–1939, Oct. 2005. doi: 10.1785/0120040210.